

TRANSFORMATION OF THE CSU–CHILL RADAR FACILITY TO A DUAL-FREQUENCY, DUAL-POLARIZATION DOPPLER SYSTEM

BY FRANCESC JUNYENT, V. CHANDRASEKAR, V. N. BRINGI, S. A. RUTLEDGE,
P. C. KENNEDY, D. BRUNKOW, J. GEORGE, AND R. BOWIE

The CSU–CHILL radar can now make simultaneous polarimetric measurements at S and X bands to advance the understanding of precipitation processes.

The Colorado State University–University of Chicago–Illinois State Water Survey (CSU–CHILL) National Radar Facility (Brunkow et al. 2000) located in Greeley, Colorado, is a research facility operated by CSU, under the sponsorship of the National Science Foundation (NSF) and CSU. The CSU–CHILL radar has recently gone through a major transformation to add support for simultaneous dual-wavelength (S and X bands), dual-polarization

(H and V) radar operation, as well as high polarization purity S- or X-band stand-alone operations (with S band being the portion of the electromagnetic spectrum comprised inside the 2–4-GHz interval, X band being the portion inside the 8–12-GHz interval, and H referring to a linearly polarized electromagnetic wave with its electric field confined on the horizontal plane, and V referring to a linearly polarized electromagnetic wave with its electric field confined on the vertical plane). This transformation process started with the installation of a low-sidelobe dual-offset Gregorian antenna capable of supporting three different feeds (S band, X band, and simultaneous S and X band all with dual-polarization capability) and culminated with the development and installation of a separate X-band channel dual-polarization radar system. This work had multiple scientific and engineering motivations, ranging from the development of specific dual-wavelength techniques and X-band algorithms that could be validated with collocated S-band data to the observation of a variety of weather phenomena at high spatial resolution and with high polarization purity.

In general, multiple-wavelength radar systems rely on the fact that a given hydrometeor will have

AFFILIATIONS: JUNYENT, CHANDRASEKAR, AND BRINGI—Department of Electrical and Computer Engineering, Colorado State University, Fort Collins, Colorado; RUTLEDGE, KENNEDY, BRUNKOW, GEORGE, AND BOWIE—Department of Atmospheric Science, Colorado State University, Fort Collins, Colorado

CORRESPONDING AUTHOR: Francesc Junyent, Electrical and Computer Engineering, Colorado State University, 209 Campus Delivery, Fort Collins, CO 80525
E-mail: francesc@engr.colostate.edu

The abstract for this article can be found in this issue, following the table of contents.

DOI:10.1175/BAMS-D-13-00150.1

In final form 27 August 2014
©2015 American Meteorological Society

a different scattering behavior depending on the wavelength at which it is illuminated, as the relative size of the scatterer with respect to the illuminating wavelength dictates the scattering regime. A small scatterer (i.e., one that is small compared to the illuminating wavelength) will operate in the Rayleigh regime, and one that has a size comparable to the wavelength (or larger) will enter the Mie regime. In addition, shorter wavelengths experience increasing attenuation when propagating through rain. All of these mechanisms are leveraged to infer something about the medium through which the radar waves are propagating.

Earlier dual-wavelength systems were motivated by hail detection and liquid water content estimation. The initial dual-frequency application appears to be hail detection based on multiple wavelength observations of a hailstorm in England (Atlas and Ludlam 1961). The underlying idea was that the scattering signal of the shorter wavelength radar would enter the Mie region before the signal of the longer wavelength radar would, when suitably large hailstones were being observed. In rain, both wavelengths would be in the Rayleigh regime (except for the larger raindrops over 3 mm in diameter), and with proper system calibration the two reflectivities should match (except for the impact of attenuation at the shorter wavelength). Estimation and removal of attenuation at the shorter wavelength (X band in this era) proved to be a difficult problem. This caused Eccles and Atlas (1973) to propose using the range derivative of the Z_s/Z_x power ratio (where $DWR = Z_s/Z_x$ is defined as the dual-wavelength ratio, with Z_s being the radar reflectivity at S band and Z_x being the radar reflectivity at X band) to identify hail boundaries. It was thought that the location of a sharp negative $d(DWR)/dr$ range derivative would accurately mark the far edge of the hail shaft. Additional experience with the derivative method resulted in rather confusing results. Jameson and Srivastava (1978) eventually showed that range variations in hailstone diameter and/or water coating could also cause significant fluctuations in the $d(DWR)/dr$ derivative. From this point on, the derivative method was abandoned and the basic attenuation-corrected DWR was used for hail detection. One of the first major applications of this dual-frequency hail signal was in an analysis of hail growth in a National Hail Research Experiment (NHRE) storm using CP2 data (Jameson and Heymsfield 1980) (CP2 was a dual-wavelength S- and X-band research radar built and operated by the National Center for Atmospheric Research that initially used separate pedestals and antennas for each frequency). Rinehart

and Tuttle (1982) argued that pattern-matching artifacts had the potential to bias the hail signal. CP2 converted to the X-band antenna(s) being mounted on the S-band pedestal in the 1980s, and in this configuration, attenuation-corrected DWR power ratio data were included in several research results: correlations of Z_{dr} [differential reflectivity, obtained as the difference in reflectivity (dBZ) at horizontal and vertical polarization] and dual-frequency indication of hail (Bringi et al. 1986b), hydrometeor identification in an evolving microburst [Microburst and Severe Thunderstorm (MIST) Project; Tuttle et al. 1989], and hail patterns in a range–height indicator (RHI) scan (Herzogh and Jameson 1992).

While dual-wavelength hail identification methods depended upon Mie scattering, efforts to estimate liquid water content (LWC) from differential attenuation at S and X bands worked best in all liquid conditions when Rayleigh scattering was present at both frequencies (Eccles and Mueller 1971). Eccles (1979) also proposed a method of using dual-frequency data to estimate rain rates. The effects of Mie scattering are significant enough that Gaussiat et al. (2003) used a three-frequency approach (S, Ka, and W bands) to improve LWC estimation in RHIs through rain showers. Frequency pairs shorter than the S–X combination used by CSU-CHILL have also been used in recent years for dual-frequency applications. As some examples, Vivekanandan et al. (2001) used X and Ka bands for the detection of supercooled water to identify aircraft icing hazards, and Chandrasekar et al. (2010) used Ka and Ku bands to document dual-frequency observations for Global Precipitation Measurement (GPM) ground validation.

The CSU-CHILL radar is designed to address the technical challenges posed by simultaneous dual-wavelength measurements through the use of a single-antenna feed illuminating the same reflector at both wavelengths. To maintain appropriate performance at both wavelengths, the radar undergoes periodic characterization of end-to-end system gain using calibration sphere flights and through the continuous monitoring of transmitter and receiver performance.

MOTIVATION FOR THE CSU-CHILL X-BAND COMPONENT.

The key motivating factor in the addition of the X-band component was the enhanced resolution achievable by the CSU-CHILL offset feed antenna at X band through its capability to accommodate different feedhorn units (S band, X band, and simultaneous S and X bands all with dual-polarization capability) to create single- and dual-wavelength, dual-polarization datasets. This

is a key feature of the CSU–CHILL radar and a differentiating factor from other weather radar systems. However, this is also a departure from traditional dual-wavelength radar systems with matched beams and the associated techniques developed for those. The main issue becomes the possibility of nonuniform beamfilling effects between the 1° beamwidth at S band and the 0.3° beamwidth at X band. In general though, it should be noted that it is possible to synthesize a larger 1° beam from the X-band higher-resolution data that matches the corresponding S-band beam (as demonstrated later in Fig. 12) or that one can analyze the statistical properties of the multiple X-band beams that fall inside the corresponding S-band beam (as shown in Fig. 10) as ways to determine whether such nonuniform beamfilling effects might be occurring.

Another important motivating factor is the investigation of attenuation correction schemes. With X-band radar systems becoming an increasingly popular technology, there is a continued need to address the particular issues that arise in higher-frequency systems such as range–Doppler ambiguity coupling and signal attenuation. The availability of a dual-polarization dataset at both S and X bands from coaxial beams is a new feature available to the research community that should allow improvements to be made in the post-processed X-band data fields and verified against their nonattenuated S-band counterparts (with CP2 being able to measure the linear depolarization ratio but no copolar variables at X band; Atlas 1990).

Another potential area of application of the dual-wavelength, dual-polarization CSU–CHILL dataset is in developing the capability to independently identify Mie scattering effects in the X-band data. This may be accomplished by examining the X-band polarimetric variables and verifying against the historical comparison of the X- and S-band reflectivities. Reliable identification of Mie scattering at X band versus S band could be used to estimate hydrometeor size.

The X- and S-band reflectivity difference could also be used to identify Bragg scattering (scattering caused by sharp gradients in the refractive index of the atmosphere); in clear air and/or first echo applications such as those discussed by Knight and Miller (1993), the signal extinction

challenges disappear and the difference between reflectivities at the different wavelengths can be attributed to the wavelength sensitivity to different scattering mechanisms. The dual-wavelength data collected so far have many examples of differing S- and X-band reflectivities in gust fronts, boundary rolls, etc.

Finally, another significant motivating factor was the potential X-band stand-alone capabilities. The higher spatial resolution allows studies of small-scale features, such as individual cumulonimbus clouds, gust front circulations, and microbursts, while the greater differential phase sensitivity should enhance the analysis of winter storm patterns, such as crystal growth; summer storm patterns, such as the identification of electrification morphology (Caylor and Chandrasekar 1996); and general rainfall estimation applications, especially for lighter rain rates.

DESCRIPTION OF THE CSU–CHILL RADAR SYSTEM.

The CSU–CHILL radar is housed inside an inflatable radome and uses a 9-m parabolic dual-offset reflector antenna (Bringi et al. 2011) mounted on an elevation over an azimuthal positioner system as shown in Fig. 1. The antenna is illuminated using one of three interchangeable feeds, allowing the system to operate at S and X bands and at simultaneous S and X bands as required. This level of flexibility allows better tailoring of the radar performance to the specific application and data purpose; the characteristics of the combined dual-frequency, dual-polarization feed, while good in its own metrics, are not as refined as that of the single-frequency units. The resulting antenna beams are conceptually illustrated in Fig. 2, showing the difference in beam sizes due to the use of the same reflector and subreflector apertures at the different wavelengths. Also, it is worth noting the preferred location of sidelobes in the higher elevation portion of the antenna pattern to



FIG. 1. CSU–CHILL National Weather Radar Facility located near Greeley.

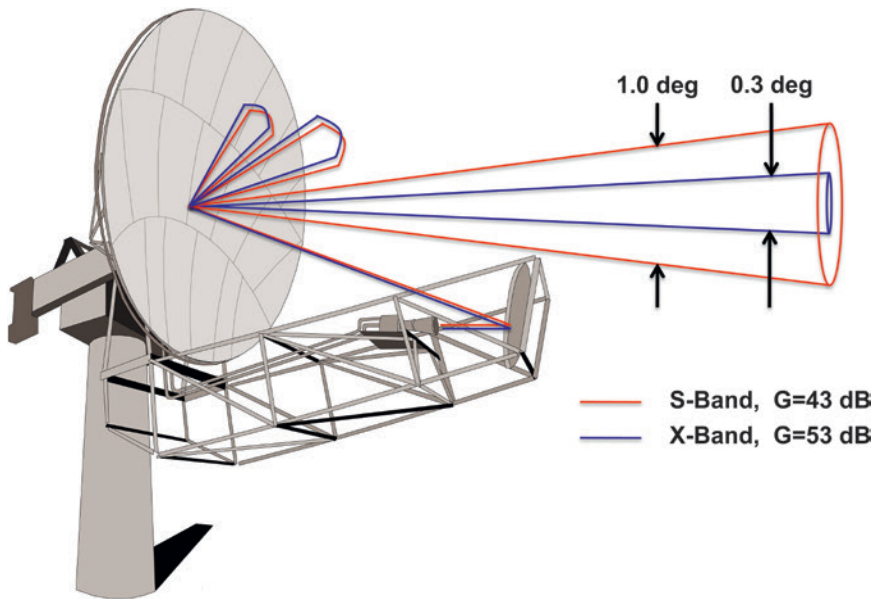


FIG. 2. Illustration of CSU-CHILL radar coaxial antenna beams. The S-band antenna beam has a gain of 43 dB and a beamwidth of 1.0°, whereas the X-band antenna beam has a gain of 53 dB and a beamwidth of 0.3°.

minimize returns from ground clutter. This is a result of the dual-offset Gregorian reflector geometry of the CSU-CHILL radar antenna. Traditional center-fed reflector antennas [such as those used in the National Weather Service’s network of operational Weather Surveillance Radar-1988 Doppler (WSR-88D) S-band radars, also known as the Next Generation Weather Radar (NEXRAD)] have no preferred sidelobe location and therefore cannot mitigate returns of ground clutter in that manner.

The X-band portion of the radar hardware is mounted directly on the antenna structure (see Fig. 3) to minimize waveguide lengths and to avoid the use of a waveguide rotary joint. The transmitter, duplexer, and receiver subsystems share a single enclosure (transceiver enclosure). A second enclosure houses the data acquisition and timing generation subsystems. The radar control and data streams share a single Ethernet interface that is brought to the signal processor system through a gigabit Ethernet-capable slip-ring assembly. The corresponding S-band portion of the radar hardware is located in a trailer adjacent to the radome.

The user trailer houses the X-band and S-band signal processor computers. The X-band signal processor gathers the digitized complex voltage radar data stream from the data acquisition system and the position data stream from the motion control system and computes the Doppler spectrum moments according to the system configuration. The real-time output of the signal processor is then passed to the data

archive and display servers, which are common to both the S-band and X-band systems. This allows leveraging the same tools for display and analysis of both X- and S-band data streams. Internet access to the signal processor computers allows remote control and operation of the radar through graphical user interfaces and/or command line programs, enabling overnight and unattended system operation. Figure 4 illustrates the architecture of the CSU-CHILL dual-wavelength radar.

Both the S-band and X-band portions of the

radar hardware contain provisions to maintain accurate system calibration. The S-band receiver is calibrated using an automated signal source injected at the calibration plane, whereas the S-band transmitted power is measured at the same calibration plane using a power meter. The power meter is also used to measure the signal source output power and to remove any bias in the transmitter-receiver calibration. The X-band receiver is calibrated using an onboard signal source, and a sample of the transmitted pulse is passed through the calibrated receiver to track the transmitted power on a pulse-to-pulse

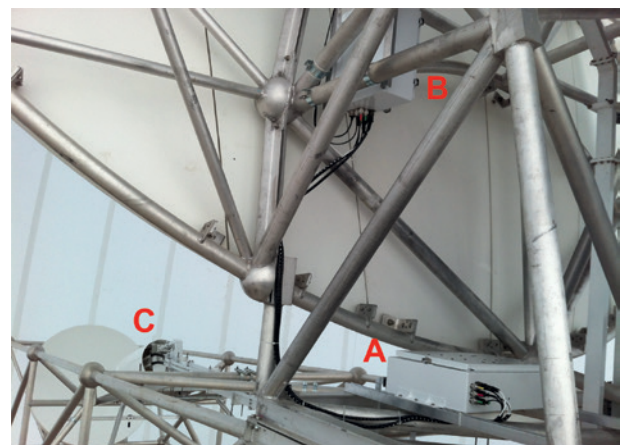


FIG. 3. CSU-CHILL radar X-band channel components: (a) the transceiver enclosure, (b) the data acquisition enclosure, and (c) the dual-frequency, dual-polarization feed.

basis. Additionally, sphere calibrations using foil-covered spheres suspended from free-flying balloons are performed routinely to check the overall system calibration.

The main characteristics of the CSU-CHILL radar both for the X-band component and the S-band component are listed in Table 1.

DATA EXAMPLES. This section presents a few data cases illustrating the CSU-CHILL radar current capabilities. These selected data cases include convective summer storms, winter storms, and nonprecipitating echoes. A larger selection of data cases can be found on the CSU-CHILL webpage (www.chill.colostate.edu) under the “Articles” tab.

Dual-frequency data for convective storms. A LOOK AT ATTENUATION. During June 2013 the CSU-CHILL radar operated in simultaneous X-band and S-band dual-frequency mode, collecting data on a number of convective storms during the CHILL Microphysical Investigation of Electrification (CHILL-MIE) project. Figures 5–7 show simultaneous data at X and S band for reflectivity (Z), copolar cross-correlation coefficient (ρ_{hv}), and differential propagation phase (ϕ_{dp}) obtained in an RHI scan through a convective storm on 29 June. Looking at the Z images, one can see that qualitatively there is very good agreement on the storm features and reflectivity levels at the higher elevation portion of the scan (above 10° elevation angle; Fig. 5). Below that, the X- and S-band measurements differ due to the presence of signal attenuation at X band beyond the higher reflectivity area in the 20-km range. The ρ_{hv} images [not corrected for the signal-to-noise ratio (SNR)] reveal that the area of higher Z is collocated with a local dip in the ρ_{hv} values (around 20 km in range, extending from 0 to 2 km in height) possibly due to some combination of depolarizing and Mie scattering effects of what could be melting graupel or hail mixed with rain. (Fig. 6; Bringi et al. 1986a). Another feature that is readily apparent is the generally slightly reduced correlation values at X band (mostly in the 0.98–0.99 range) when

compared to S band (mostly in the 0.99–1.00 range) when operating in dual-frequency mode, probably due to the lower quality of beam matching at the two polarizations at X band. This is believed to be a side effect of the dual-polarization, dual-frequency horn illuminating the antenna system, as other X-band datasets collected with the single-frequency X-band horn (as the one shown in Fig. 16) do behave as expected. The ϕ_{dp} images show the expected increase after the high Z areas with overall higher-phase excursions at X band (Fig. 7). The higher sensitivity of ϕ_{dp} at X band makes some features, such as the potential vertical alignment of particles due to electrification (roughly at 30-km range and 10-km height), easier to observe. One can also see how in the area around 20 km in range where the Z maximum is located, ϕ_{dp} at X band goes through a local maximum possibly due to backscatter differential phase owing to scattering off melting ice particles and/or large raindrops (Trömel et al. 2013).

The availability of simultaneous reflectivity measurements at X and S bands offers the possibility of using the unattenuated S-band measurement as a constraint for the attenuation correction algorithm applied to the X-band data. To do so successfully, one must be certain that no residual bias exists between the measured X- and S-band reflectivities (i.e., the measured data are properly calibrated). To assess that potential bias as shown in Fig. 8, the data from the top portion of the previously shown Z scan are selected (over 10° in elevation in Fig. 5), and a two-dimensional histogram of Z values at X and S band between 10 and

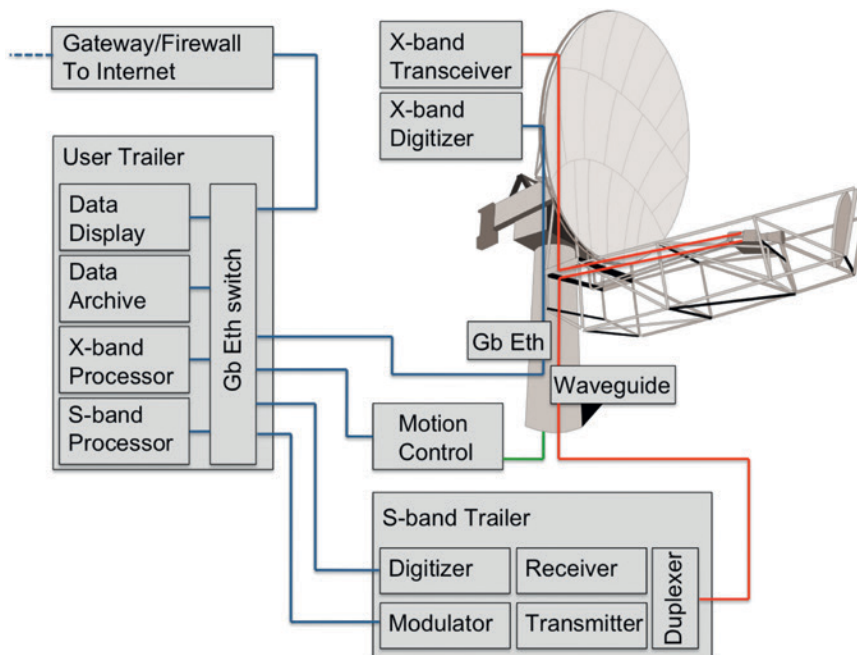


FIG. 4. CSU-CHILL dual-frequency radar architecture.

TABLE 1. CSU–CHILL dual-frequency radar system main specifications.

| Parameter | S band | X band |
|---------------------------------------|--|-------------------|
| Antenna | | |
| Reflector type | 8.5-m dual-offset Gregorian parabolic | |
| Feed type | Scalar, symmetric orthomodal transducer (OMT) | |
| Polarization | Linear H and V | |
| Gain (dBi) | 43 | 53 |
| Beamwidth (°) | 1.0 | 0.3 |
| Sidelobe level (dB) | <−33 | <−36 |
| Cross-polarization level (dB) | <−35 | <−35 |
| Scan type | PPI (360° sector), RHI, fixed pointing, vertically pointing | |
| Scan rate | <18° s ^{−1} | |
| Transmitters | | |
| Frequency | 2.725 GHz | 9.41 GHz ± 30 MHz |
| Type | Dual Klystron | Magnetron |
| Power max | 1 MW | 25 kW |
| Transmit modes | Single polarization, simultaneous, alternating | Simultaneous |
| Duty cycle (%) | 0.16 | 0.16 |
| PRF max (kHz) | 1.25 | 2.00 |
| Receivers | | |
| Sensitivity (dual-wavelength mode) | −15 dBZ, 10 km | −15 dBZ, 10 km |
| Noise figure (dB) | 3.4 | 4.0 |
| Dynamic range (dB) | 80 | 90 |
| Digitizer bits | 14 | 14 |
| Range sampling (m) | 30–150 | 1.5–192 |
| Signal processing and products | | |
| Processing modes | Pulse pair, spectral clutter filter, second-trip suppression, dual-Doppler velocity unfolding | |
| Polarization processing | Hydrometeor ID, attenuation correction, <i>KDP</i> estimation | |
| Data products | Z , Z_{DR} , V , W , ρ_{HV} , NCP , ϕ_{DP} , K_{DP} , SNR , (LDR, ρ_{CX} for S-band only) | |

35 dBZ is created. The data points in the histogram are probably mostly ice particles, although supercooled liquid water cannot be ruled out. All histogram data points below a threshold (at least four occurrences for this particular dataset) are eliminated, so that rare occurrences (points affected by attenuation, dissimilar scattering mechanisms, etc.) do not bias the sample. After that, the mean value of each one-dimensional histogram of X-band reflectivity values per S-band reflectivity bin is obtained (shown as plus sign points in Fig. 8), and a regression line is fit through the resulting mean values. The obtained regression line shows that the two Z datasets are well correlated (with slope $m = 1.0006$) and that there is negligible bias (with offset $n = -0.0040$). Additionally, the standard deviation is calculated and found to be slightly over 2 dB.

Once established that the X and S band datasets are well correlated and unbiased, attenuation correction can be attempted. As previously mentioned, the S-band measurement can be used as a constraint for the attenuation correction algorithm applied to the X-band data. This is expressed in mathematical form in Eq. (1) below, where $Z_H^S(r)$ is horizontal polarization reflectivity at S band, $Z_H^X(r)$ is horizontal polarization reflectivity at X band, $A(r, \alpha)$ is specific attenuation as defined in Eq. (7.143) in Bringi and Chandrasekar (2001), r is range, and α is the total attenuation (dB) at the maximum range considered:

$$\min_{\alpha} f(\alpha) = \left\| Z_H^S(r) - [Z_H^X(r) + A(r, \alpha)] \right\|. \quad (1)$$

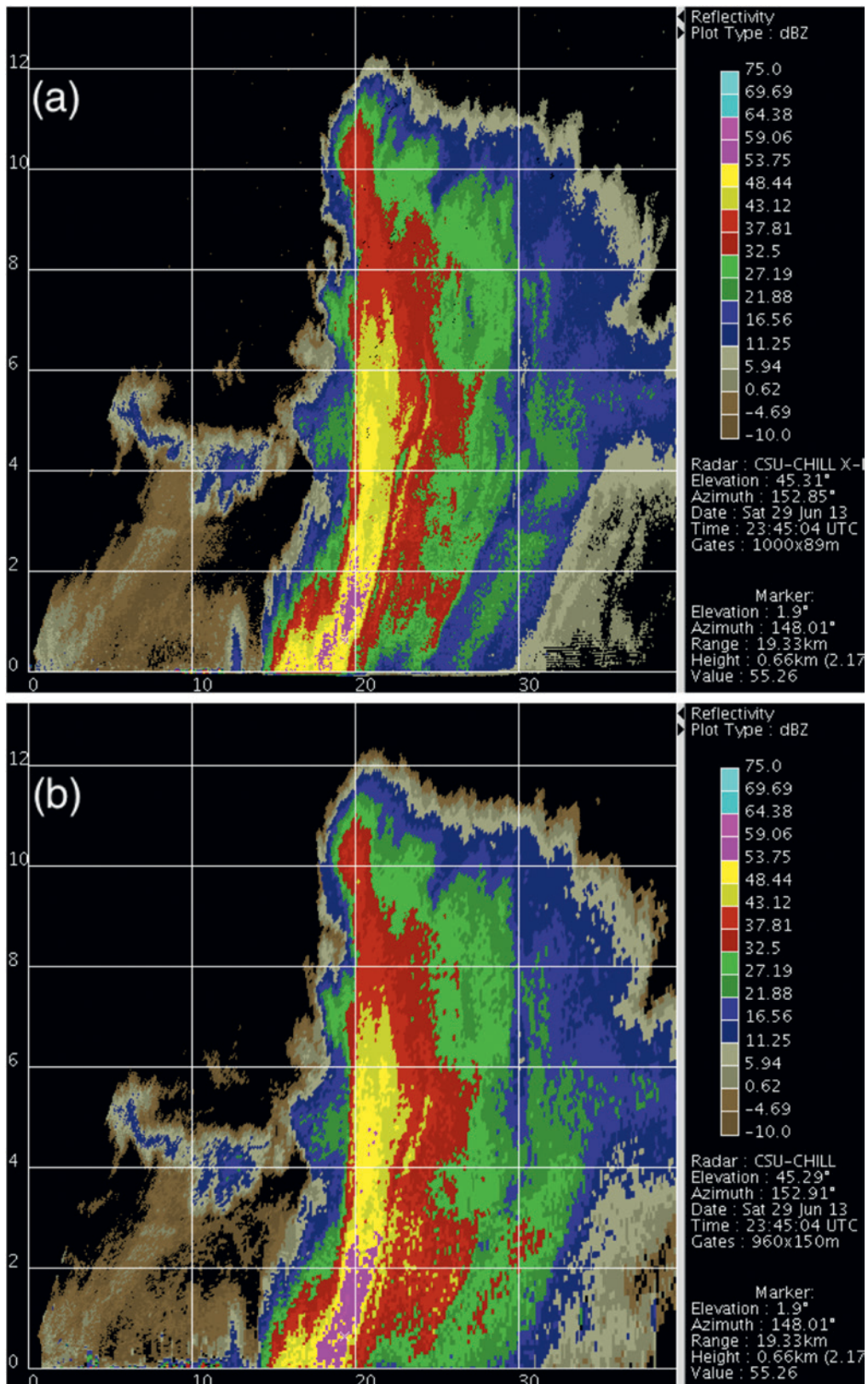


FIG. 5. CSU-CHILL dual-wavelength Z comparison on 29 Jun 2013: (a) uncorrected X band and (b) S band. Note the generally good agreement on the storm features and Z levels at the higher elevation angles, and how they start to differ at lower angles due to the presence of attenuation from 20 km onward.

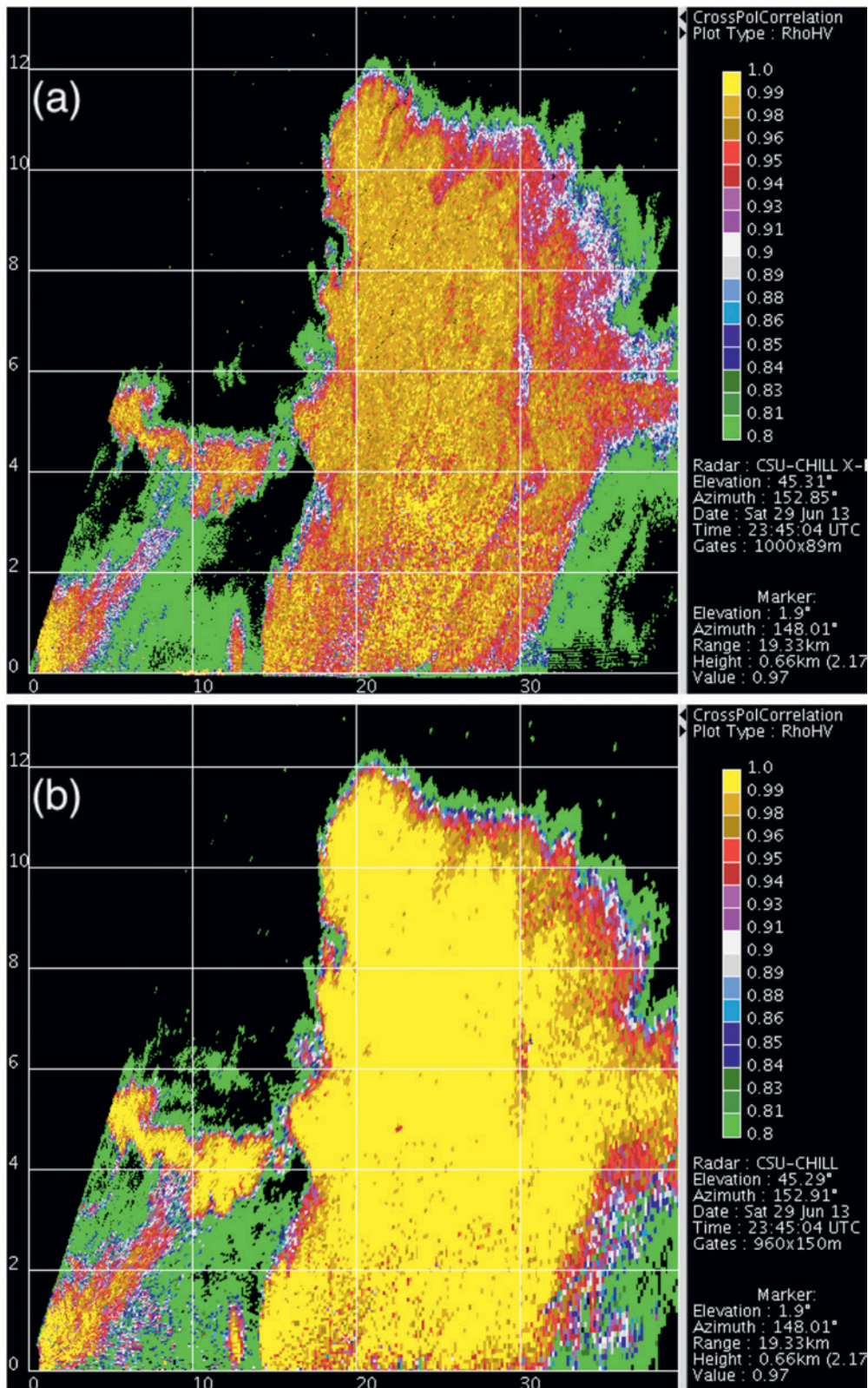


FIG. 6. CSU-CHILL dual-wavelength ρ_{hv} (not corrected for SNR) comparison on 29 Jun 2013: (a) X band and (b) S band. Note that the area of higher Z in the previous figure is collocated with a local dip in the ρ_{hv} values at both frequencies (around 20 km in range, extending from 0 to 2 km in height). This could be due to some combination of depolarizing and Mie scattering effects of what could be melting graupel or hail mixed with rain.

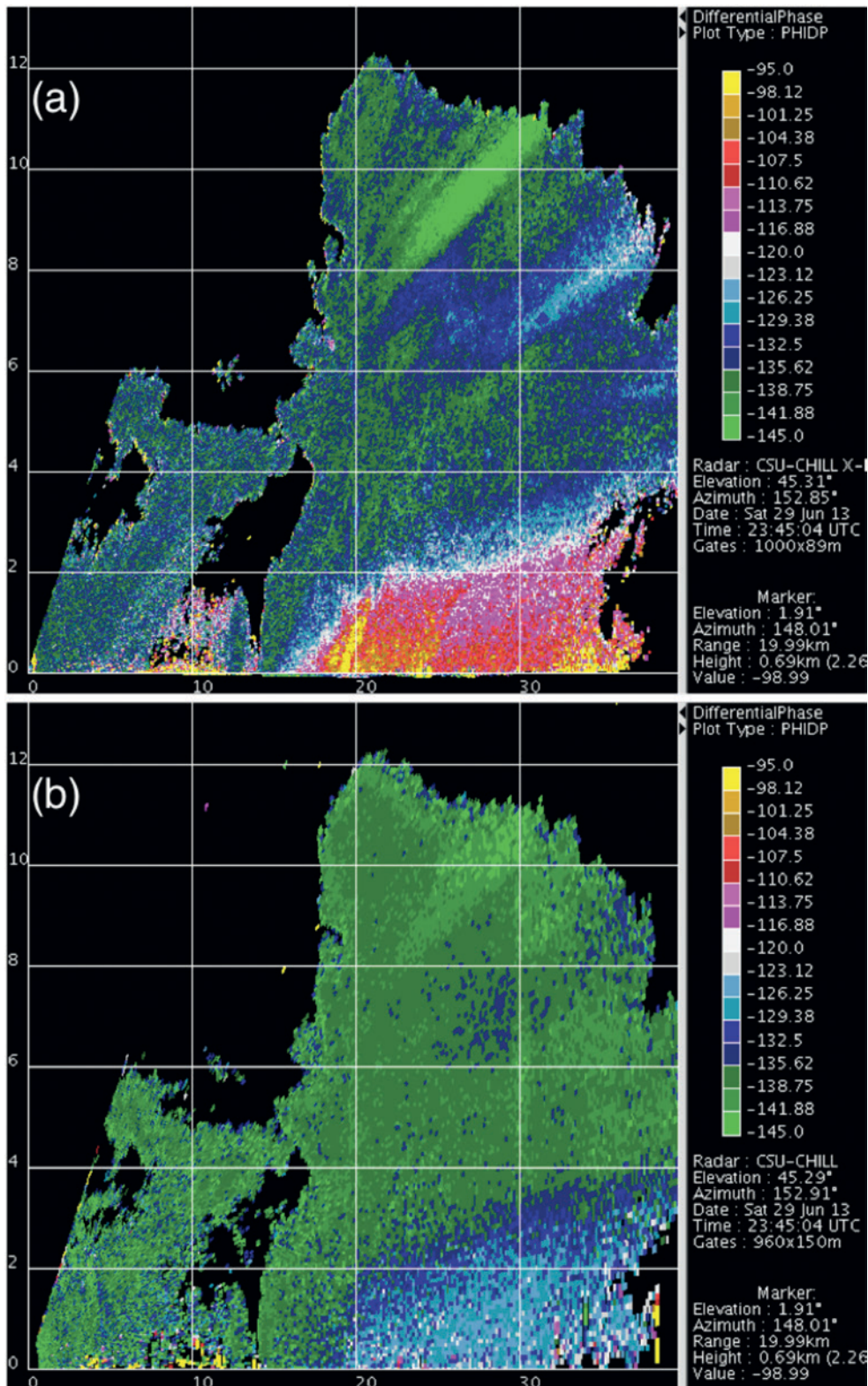


FIG. 7. CSU-CHILL dual-wavelength ϕ_{dp} comparison on 29 Jun 2013: (a) X band and (b) S band. Note the expected increase after the high Z areas, with generally higher phase excursions at X band. Also, the higher sensitivity at X band makes some features easier to distinguish, such as potential vertical alignment of particles due to electrification (green streak extending through 30 km in range and 10 km in height), and the X-band local maximum at 20 km is possibly due to differential phase shift upon backscattering.

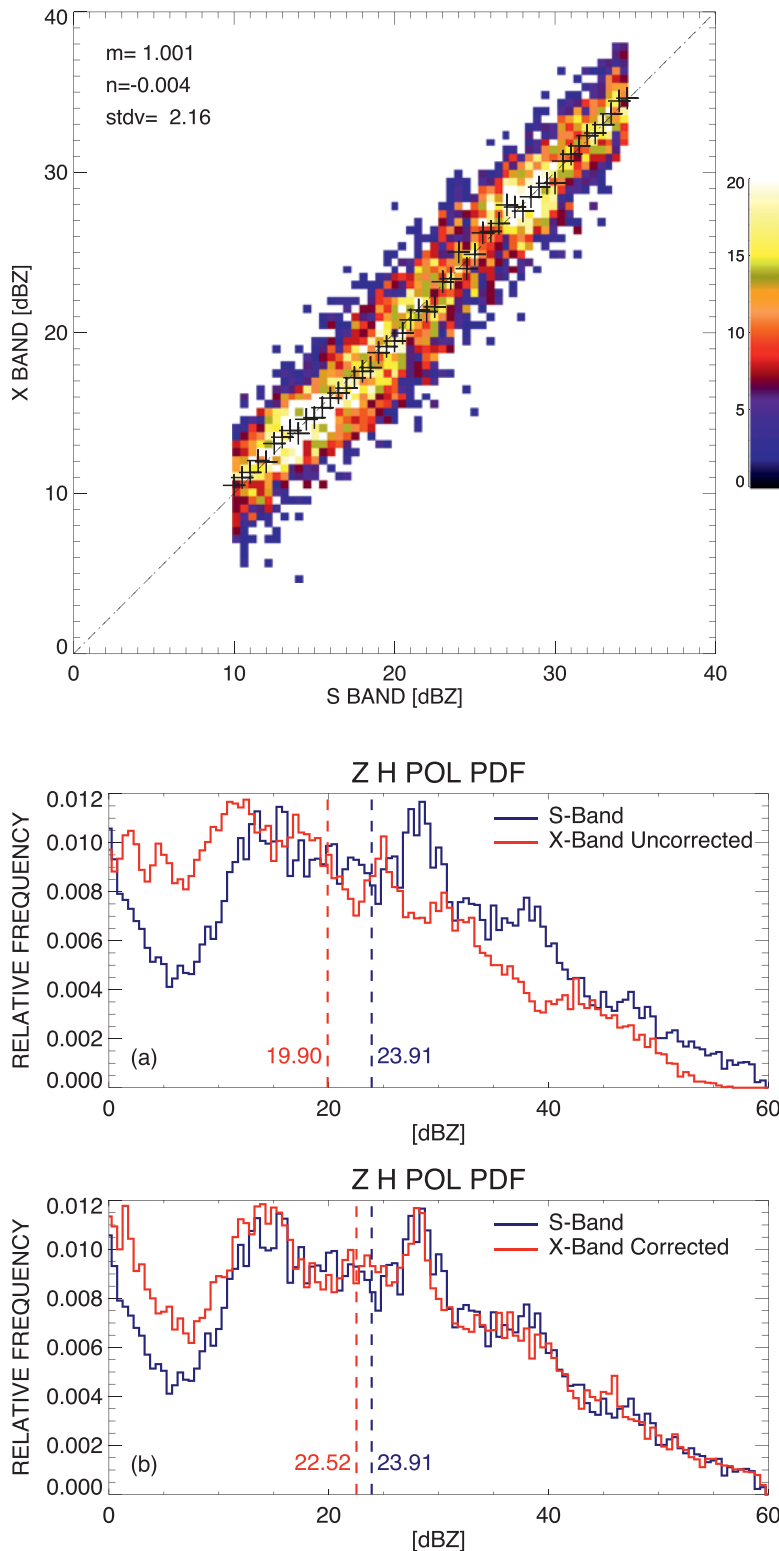


FIG. 8. Residual bias and correlation of intrinsic reflectivity values (not corrected for attenuation) at X and S bands. The data employed are obtained from the top portion (over 10° in elevation) of the previously shown reflectivity scan (Fig. 5), and it may contain a mix of ice and water particles. Color points correspond to thresholded 2D Z histogram (see color scale indicating number of occurrences); mean value of each 1D histogram of X-band reflectivity values per S-band reflectivity bin is shown as a plus sign point; and dotted line is the resulting fit to the mean values with slope m , offset n , and standard deviation $stdv$. The fit shows that the two datasets are well correlated and unbiased, suitable for further joint processing such as attenuation correction.

Equation (1) is a nonlinear least squares problem that can be solved for α using an algorithm such as Levenberg–Marquardt (Levenberg 1944; Marquardt 1963). The result of applying this attenuation correction procedure to the X-band data can be seen in Fig. 9. Figure 9a shows the normalized histogram of the measured Z at S band overlaid onto the normalized histogram of the measured Z at X band, as a way to illustrate the effect of the correction algorithm. In Fig. 9a it can be seen how the number of occurrences for the higher reflectivity values at X band is underestimated, while the number of occurrences for the lower values is overestimated when compared to S band. This is the effect of signal attenuation at X band, shifting points from their higher intrinsic reflectivity values to lower attenuated values. Figure 9b shows the same normalized histogram comparison after correcting for attenuation in the X-band Z, showing excellent agreement between the two datasets.

A more detailed ray comparison between X- and S-band measurements is shown in Fig. 10. A data ray at 1.95° elevation angle is selected,

FIG. 9. S- and X-band Z normalized histogram comparison (a) before and (b) after attenuation correction at X band, using the datasets shown in Fig. 5. One can see how the attenuation correction process shifts X-band-attenuated lower reflectivity points to their estimated higher reflectivity values. Dashed vertical lines indicate the mean value for each histogram, giving a quantitative indication of the improved agreement between datasets after attenuation correction.

which goes through the higher reflectivity portion of the storm shown in Fig. 5. Figure 5a shows the measured Z at X and S bands, together with the attenuation-corrected Z at X band. The attenuation-corrected Z at X band shows almost 10 dB of total attenuation. Finally, Fig. 5b shows ϕ_{dp} for X and S band, both as measured and after fitting a spline as described in Wang and Chandrasekar (2009). The S-band data have the expected smooth monotonic upward trend, whereas the X-band data exhibit a clear local maximum around the 20-km range possibly due to differential phase shift upon backscattering. The backscatter differential phase is generally indicative of Mie scattering effects, as otherwise suggested by the collocated appearance of reflectivity values in excess of 50 dBZ and a local drop of the copolar cross-correlation coefficient to values around 0.9, which could be associated with the presence of large scatterers such as wet graupel or hail. The total phase excursion at X band is roughly 3 times the phase excursion measured at S band as expected for Rayleigh scatterers.

A LOOK AT DUAL-WAVELENGTH RATIO. The availability of simultaneous reflectivity and polarimetric measurements at X and S bands allows analyzing DWR together with its associated polarimetric signatures. Figure 11a shows a low-elevation angle (0.47°) plan position indicator (PPI) of S-band reflectivity obtained on 26 July 2013 and the cell of interest being centered at ($X = 10, Y = 60$ km) from the radar. The dashed line represents the radial along which RHI data are shown. The cell is intense with Z_s reaching a maximum >65 dBZ. Figure 11b shows the RHI of Z_s with 60 dBZ extending to around 8 km AGL. Figure 11c shows the DWR (dB) RHI data. Note the strong X-band attenuation [path-integrated attenuation (PIA)] in excess of 50 dB (along a radial that includes the open circle mark, elevation angle of 0.47°). Aloft the PIA is much lower around 15 dB (e.g., along a radial that includes the open circle mark, elevation angle of 5.3°). Figure 12 shows the range profile at an elevation angle of 0.47° of Z_s and Z_x (Fig. 12a) and DWR and ϕ_{dp}^x (differential propagation phase at

X band; Fig. 12b). The X-band signal is strongly attenuating with ϕ_{dp}^x increasing from -120° (at range 53 km) to -60° (at range 62 km), or an increase of 60° over the 9-km path (over a rain path, the PIA and measured ϕ_{dp}^x excursion are proportional, and the latter can be taken as a proxy for attenuation). The X-band PIA, if the path were only composed of rain, can be estimated from $PIA = 0.3 \times 60$ or 18 dB (where the coefficient of 0.3 dB degree $^{-1}$ is reasonable at X band; e.g., Park et al. 2005). However, the DWR data show an increase from 5 dB at 53 km to 45 dB at 62 km, corresponding to a PIA of 40 dB; so, it can be inferred that the excess PIA of 22 dB (40–18 dB) is due to wet hail along the path (i.e., the path is composed of heavy rain mixed with wet hail). As there is no obvious Mie hail signal in the DWR profile (i.e., there is no noticeable local departure from the general DWR trend), the wet hail diameters

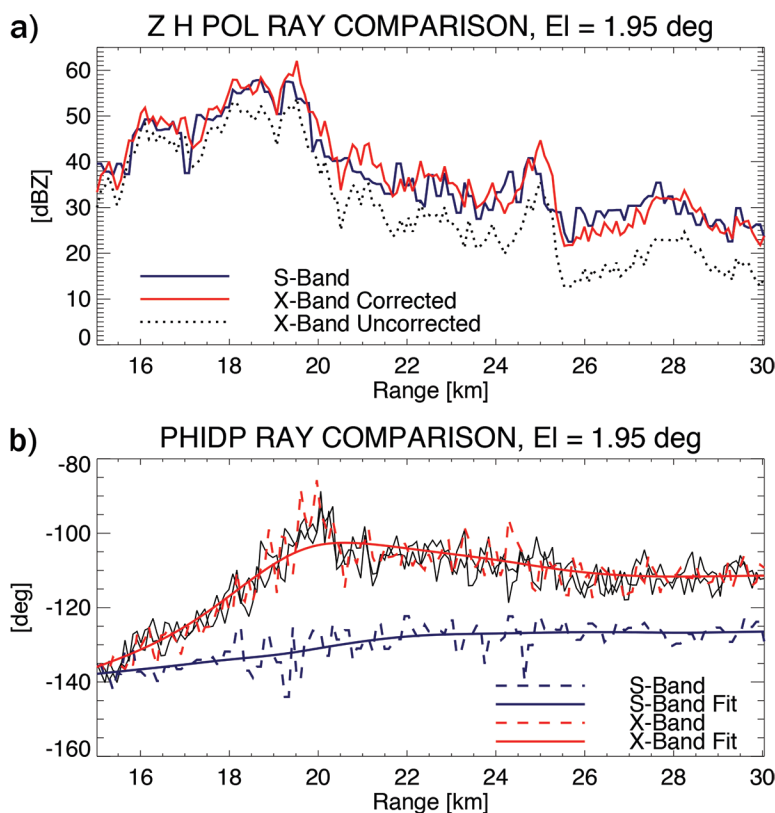


FIG. 10. S- and X-band ray comparison at 1.95° elevation angle, taken from the storm shown in the previous figures: (a) Z , showing around 10 dB of PIA and (b) ϕ_{dp} , where dashed lines show the raw measurement and solid lines show a fitted smoothing spline. To rule out any nonuniform beamfilling effect, the X-band data also show the adjacent rays at $1.95^\circ \pm 0.3^\circ$, which closely track each other and the analyzed ray. The standard deviation of the profiles is found to be approximately 2.5° for X band and 2.0° for S band. The S-band data have the expected smooth monotonic upward trend, whereas the X-band data exhibit a clear local maximum around the 20-km range, possibly due to differential phase shift upon backscattering.

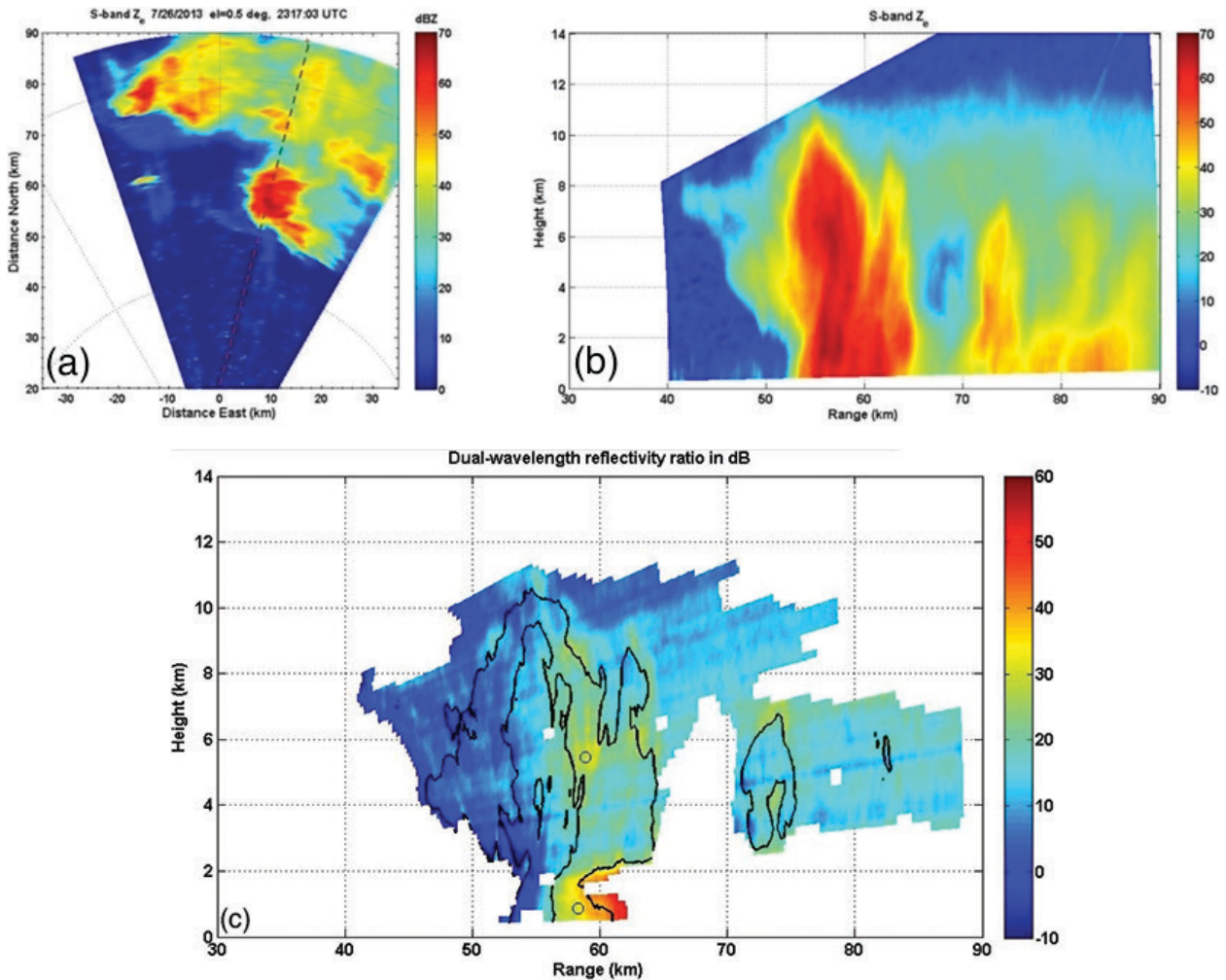


FIG. 11. Case from 26 Jul 2013. (a) PPI of Z_s at elevation angle of 0.47° . Dashed line marks the azimuthal angle along which RHI data are shown in (b) and (c). (b) RHI of Z_s along azimuthal angle of 11° [see dashed line in (a)]. (c) As in (b), but DWR is shown, together with contours of X-band reflectivity starting at 20 dBZ and incrementing by 20 dB. Circle markers are points of interest discussed in the text. Note that in (c) and Fig. 12 that the X-band data have been interpolated to the S-band range–elevation grid.

are estimated to be <1 cm. Figure 12 shows similar range profiles at an elevation angle of 5.3° of Z_s and Z_x (Fig. 12a) and DWR and X-band copolar correlation coefficient ρ_{hv} (Fig. 12b). There are several points that can be made: 1) the PIA is now reduced to 15 dB; 2) the monotonic increase in DWR with range is now “perturbed” by the Mie hail signal, whose range extent is indicated by the two-sided arrow marked with hail signal (HS) and whose values reach 10–12 dB, indicative of hail diameters of around 2 cm (Ulbrich and Atlas 1982); and 3) a significant decrease in X-band ρ_{hv} to 0.8 within the central portion of the HS, which is marked by the two-sided arrow in red. The latter reduction in ρ_{hv} is likely caused by some combination variance in hail shapes and differential backscatter phase (which could be due to wet hail) (e.g., Snyder et al. 2013).

Dual-frequency scans for a dry cold front. During the midday hours of 15 August 2012, a cold front that produced no precipitation and minimal cloud development passed the CSU–CHILL radar site while moving toward the southwest. As the front approached, the CSU–CHILL radar was operated in dual-frequency mode. To provide high temporal resolution, the antenna executed only a single 360° PPI scan at an elevation of 1° followed by two RHI sweeps aimed at the approaching front. This scan pattern gave a cycle time of 140 s to allow fine sampling of the frontal passage.

Figures 13 and 14 show a snapshot of Z and Z_{dr} at X and S bands. Convergence along the leading edge of the dry cold front enhanced the concentration of insects and debris raised from the surface, contributing to a

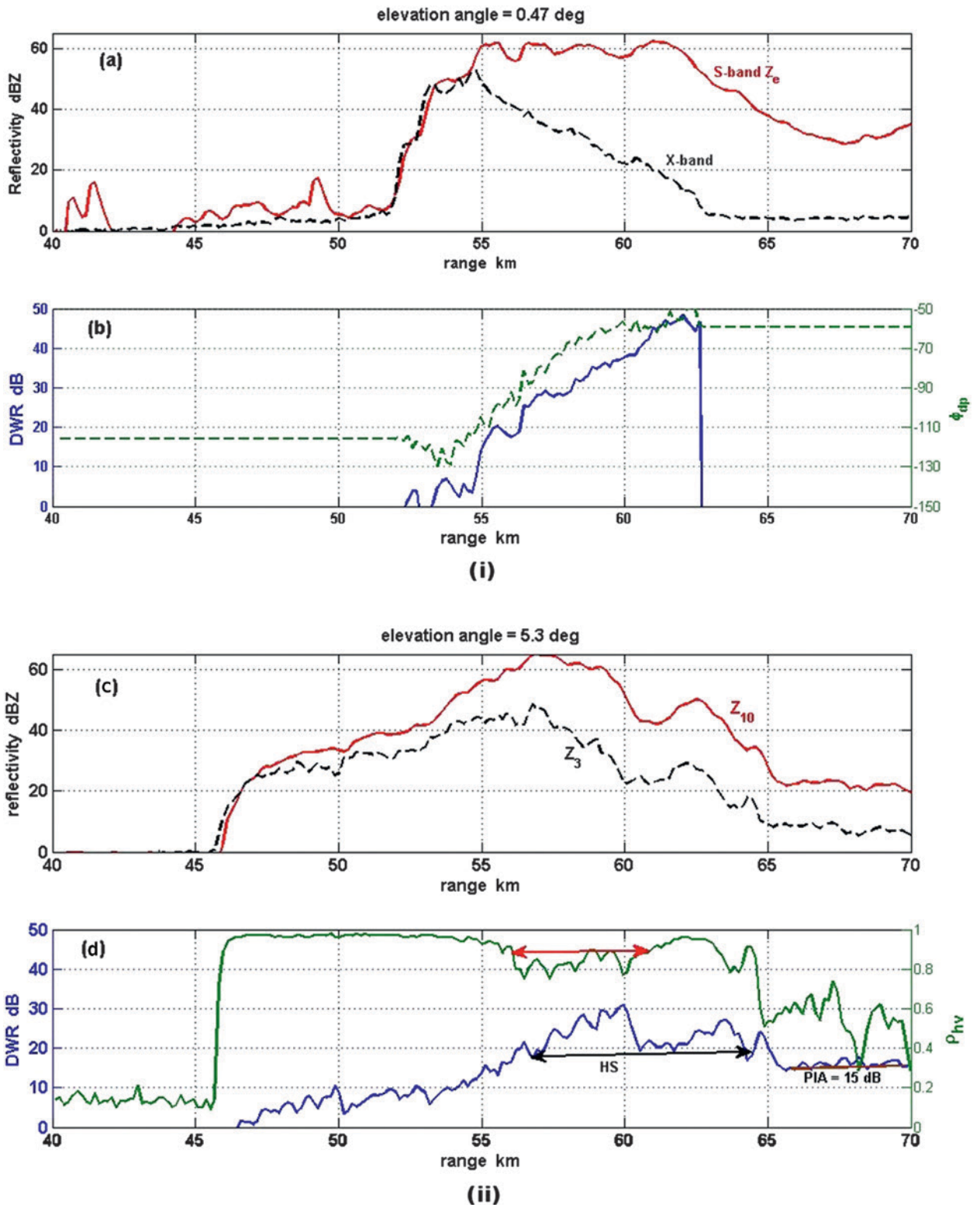


FIG. 12. (top) Range profile at elevation angle of 0.47° of (a) Z_s (solid red line) and Z_x (dashed black line) and (b) DWR (solid blue line) and X band ϕ_{dp} (dashed green line). (bottom) As in (top), but (c) Z_s (solid red line) and Z_x (dashed black line) and (d) DWR (solid blue line) and X-band ρ_{nv} (solid blue line). The double-ended horizontal red arrow marks the area of low ρ_{nv} collocated with the HS range indicated by the double-ended horizontal black arrow.

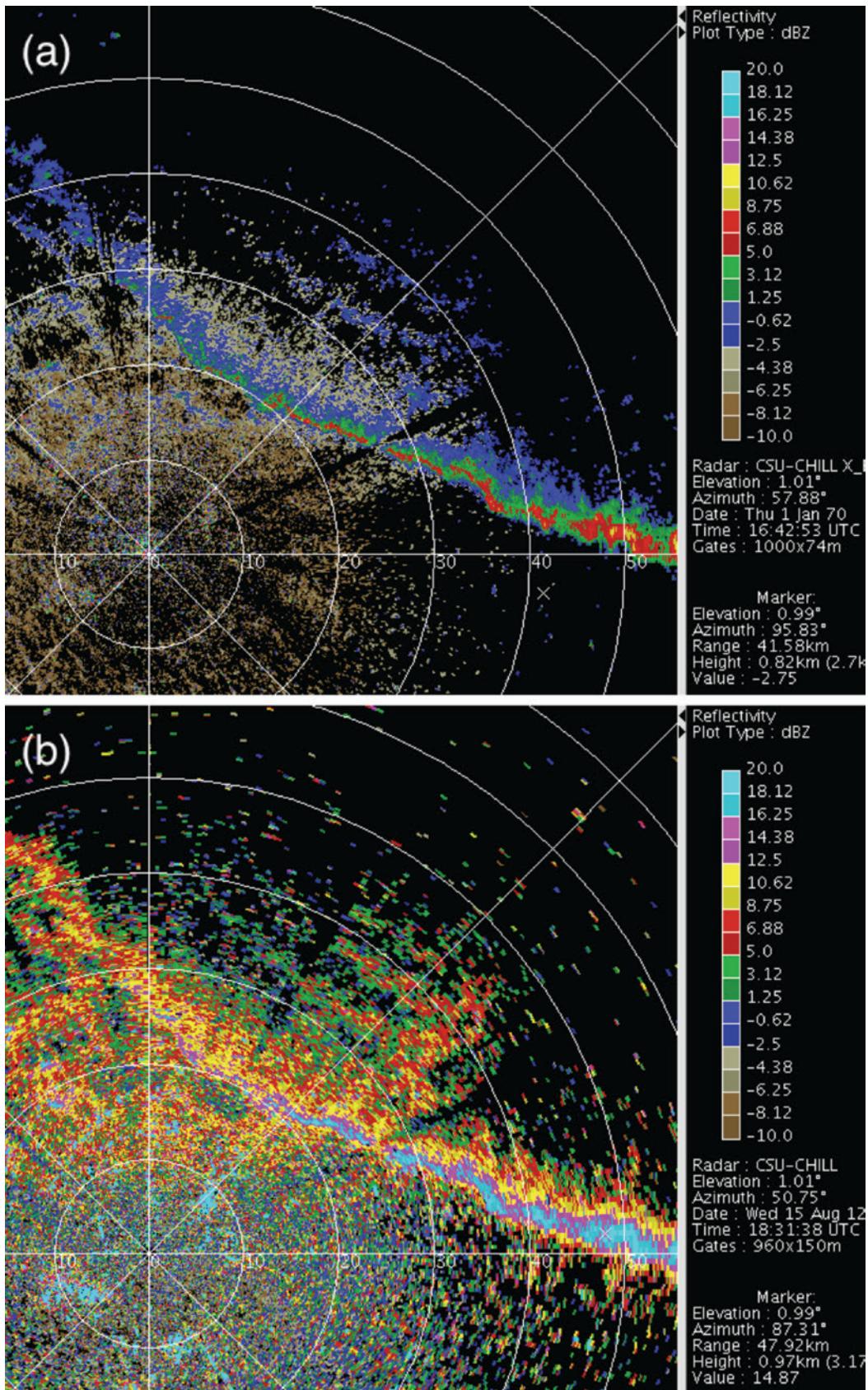


FIG. 13. CSU-CHILL dual-wavelength Z data collected during a frontal passage on 15 Aug 2012: (a) X band and (b) S band.

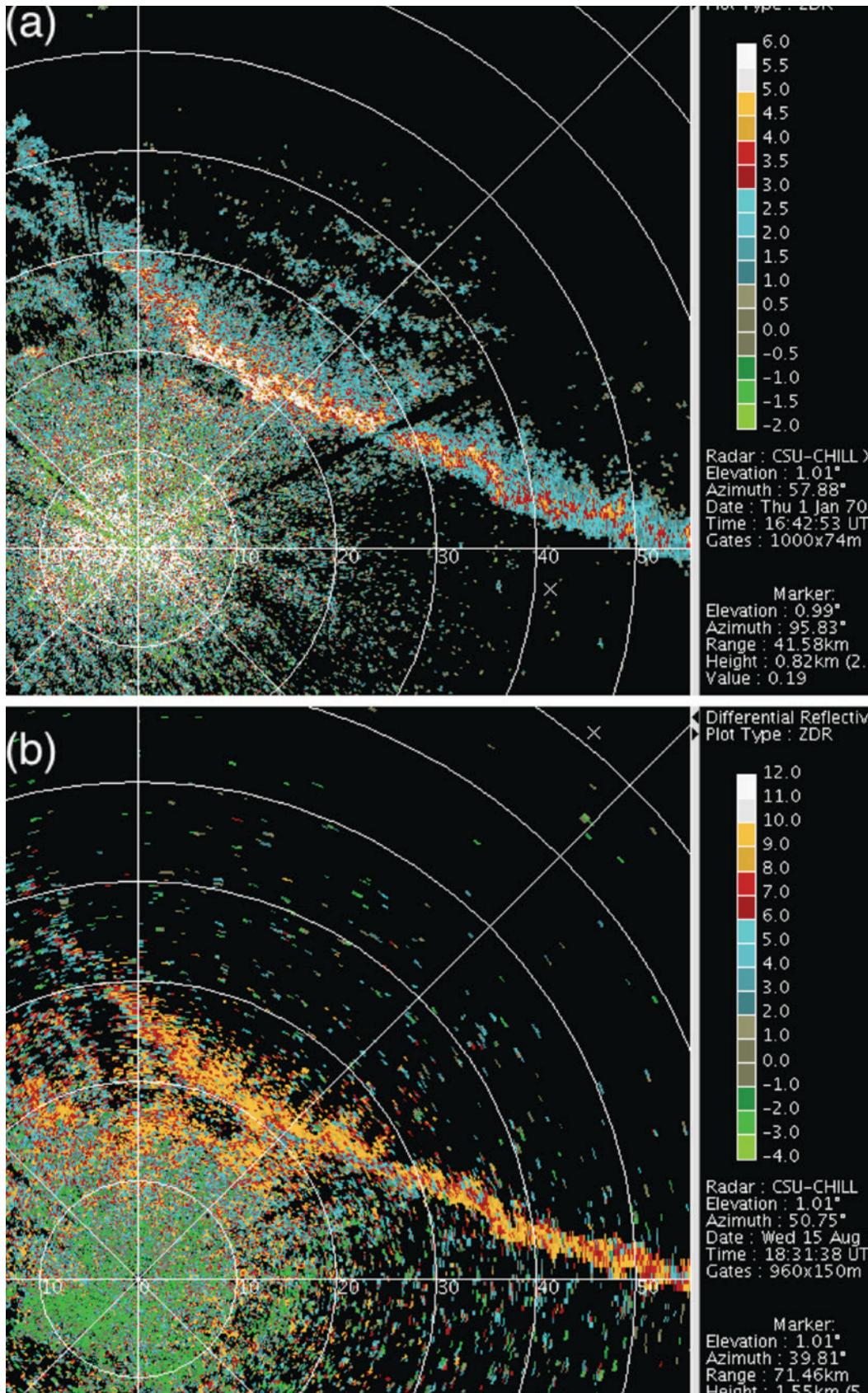


FIG. 14. CSU-CHILL dual-wavelength Z_{dr} data collected during a frontal passage on 15 Aug 2012: (a) X band and (b) S band.

thin band of maximized Z . To the rear of the front, the spatial reflectivity patterns showed indications of both open cellular and horizontal roll patterns as the thermal stability and wind shear structure changed in the postfrontal airmass. The narrow (0.3°) X-band antenna pattern and small (90 m) range depth in the X-band data improved the resolution of these echo features. The echo patterns at S band are coarser owing to the 1° beamwidth and the 150-m range gate depth. The S-band Z values are appreciably stronger than those at X band due to the larger Bragg scattering contribution at S band (Knight and Miller 1993) and possibly different scattering regimes at S band (Rayleigh) and X band (Mie) in insects (which would also contribute to larger S-band Z_{dr} values).

X-band data collected in a winter storm. From December 2012 to April 2013, the CSU–CHILL radar operated at X band only. The increased resolution and sensitivity of the higher frequency, coupled with the potentially less severe attenuation in winter precipitation make X band well suited for these types of observations. Operating with a single-frequency feed (X band only in this case) allows for obtaining higher polarization purity than when employing the dual-frequency feed. Figures 15–17 show data obtained on an RHI scan through a snowband on 15 April 2013 during the Front Range Orographic Storms (FROST) experiment (Kumjian et al. 2014). Figure 15a shows the Z structure of the snowband. A greater than 20-dBZ fall streak is readily apparent starting around 4 km in height at 45 km in range, falling toward the radar and reaching the ground at an approximate range of 20 km. Term Z_{dr} (Fig. 15b) shows near-zero values in the area corresponding to the higher Z values, indicative of snow aggregates. In the areas corresponding to lower Z , Z_{dr} has positive values in the 0.5–1.5-dB range, possibly due to more pristine crystals. It is worth noting the region around 4 km in height at 35 km in range where Z_{dr} presents slightly higher values (over 1.5 dB). Figure 16 shows the corresponding ϕ_{dp} and specific propagation phase (K_{dp}) data (Figs. 16a,b, respectively). The higher sensitivity at X band allows for more clearly distinguishing the upward trend of the ϕ_{dp} phase in a relatively weak echo environment (maximum Z values are below 30 dBZ). Term K_{dp} reveals an area of higher values that is located just below the area of higher values of Z_{dr} , suggesting the formation of more pristine ice crystals above the area of higher Z values. This could be an indication of an ice crystal growth mechanism that is followed by the aggregation and descent of the heavier snowflakes (Kennedy and Rutledge 2011; Andrić et al. 2013). Figure 17a shows the

corresponding Doppler velocity (V) field. The wind shear structure (toward the radar at heights roughly below 2.5 km, away in the layer above that up to 4 km) is consistent with the snowfall streak trajectory. Also, convergence supportive of an updraft is present in the lower portion of the precipitation-generating cell at an approximate range of 47 km and a height of 2.3 km AGL. Figure 16b shows the ρ_{hv} data. It is readily apparent that the achieved values in the higher signal-to-noise ratio areas for X band only (Fig. 16b) are above those achieved in the previously presented simultaneous X- and S-band dataset (Fig. 6a), as the limiting factor is the antenna feed performance.

X-band data collected in a tornadic storm. In the early afternoon of 18 June 2013, a tornado developed over the Denver International Airport while CSU–CHILL was in operation during the National Science Foundation (NSF)-sponsored Research Experiences for Undergraduates (REU) 2013 project. Figure 18 shows a general view of the storm and a detailed view around the tornado signature of Z and V . The selected X-band scan was taken at an elevation of 0.5° and shows a very well-defined hook-echo signature with an approximate diameter less than 2 km at a range near 70 km directly south of the radar, made possible owing to the very small antenna beamwidth at X band (0.3°). The V field shows a tight azimuthal shear couplet in the Doppler velocity collocated with the hook echo. Because the CSU–CHILL X-band radar channel operates with a dual-PRF scheme similar to that described in Bharadwaj et al. (2010), it allows for resolving Doppler velocities close to $\pm 24 \text{ m s}^{-1}$ while maintaining an unambiguous range of 100 km.

CONCLUSIONS. This study describes the successful transformation of the CSU–CHILL National Radar Facility to a diverse radar system capable of operating at S band only, X band only, and simultaneous S and X bands, all providing a full suite of Doppler and polarimetric measurements. The X-band component features a high-gain, 0.3° beamwidth antenna providing unprecedented resolution at that wavelength. The capability of changing the operational mode among these three configurations (in roughly 24 h) provides optimization for the user-specified application. The S-band-only mode provides maximum sensitivity at S band with superb cross-polarization isolation and polarimetric data quality. The X-band-only mode provides superior data quality at X band and maximum sensitivity. The dual-frequency mode, of course, provides simultaneous S- and X-band polarimetric measurements with slightly reduced sensitivity at

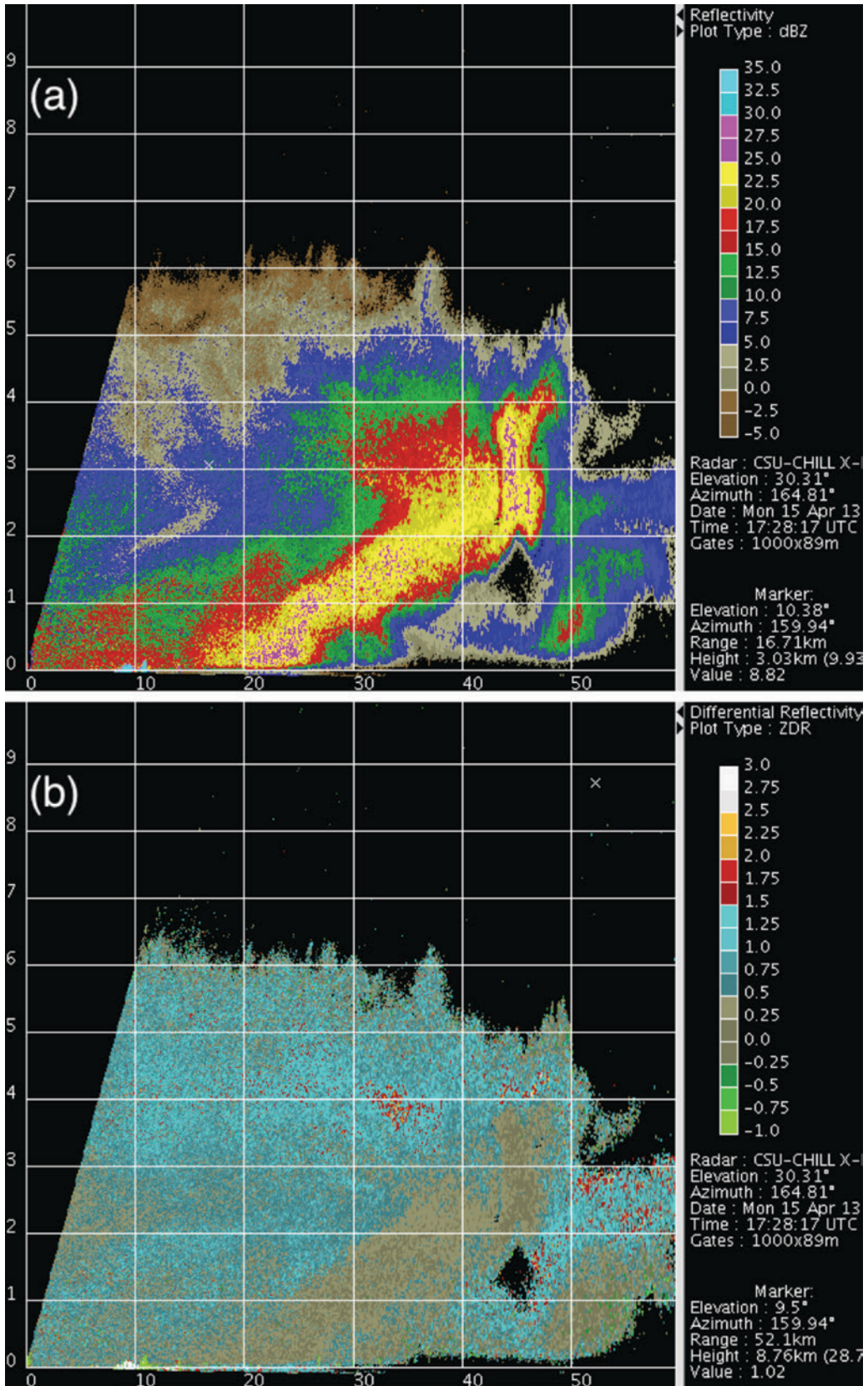


FIG. 15. CSU-CHILL X-band data collected through snowband on 15 Apr 2013: (a) reflectivity showing a higher intensity (above 20 dBZ) fall streak and (b) Z_{dr} , showing near-zero values in the area corresponding with the higher Z values as snow aggregates.

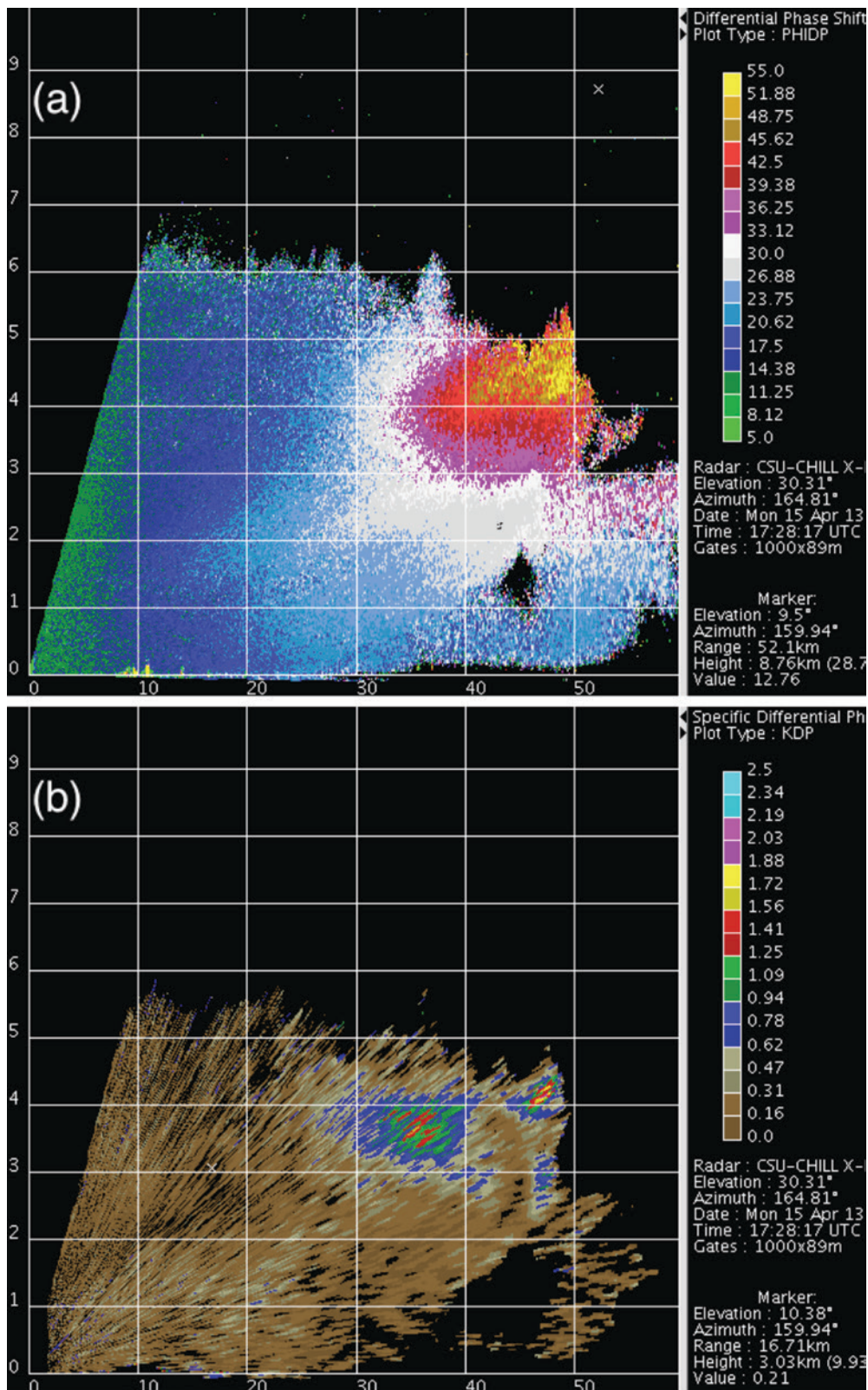


FIG. 16. CSU-CHILL X-band data collected through snowband on 15 Apr 2013: (a) ϕ_{dp} , showing a clear upward trend in a relatively weak echo environment (maximum Z values are below 30 dBZ), and (b) K_{dp} , revealing an area of higher values that is located above the higher values of Z_{dr} , suggesting the formation of more pristine ice crystals above the area of higher Z values.

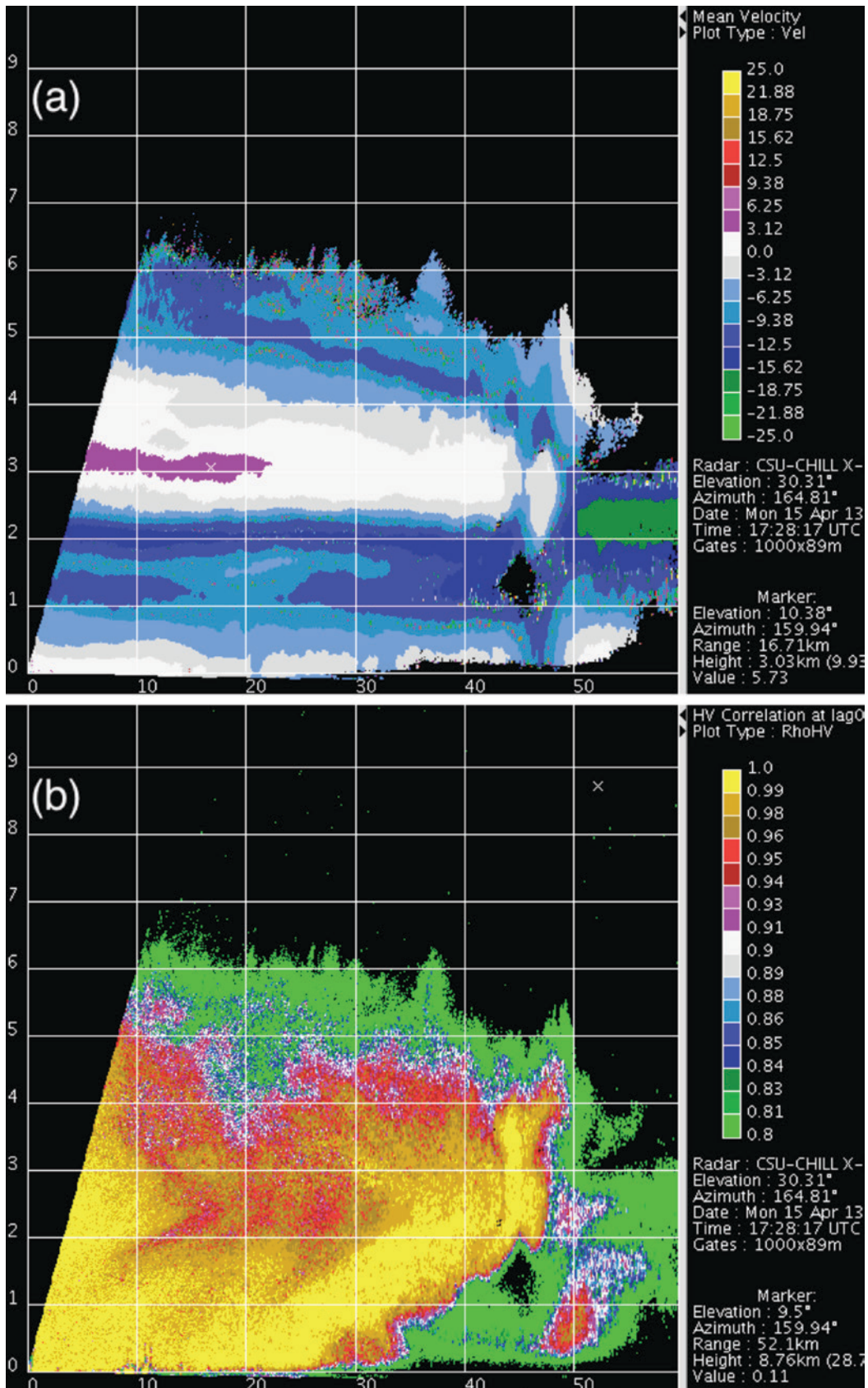


FIG. 17. CSU-CHILL X-band data collected through snowband on 15 Apr 2013: (a) V and (b) ρ_{hv} (not corrected for SNR).

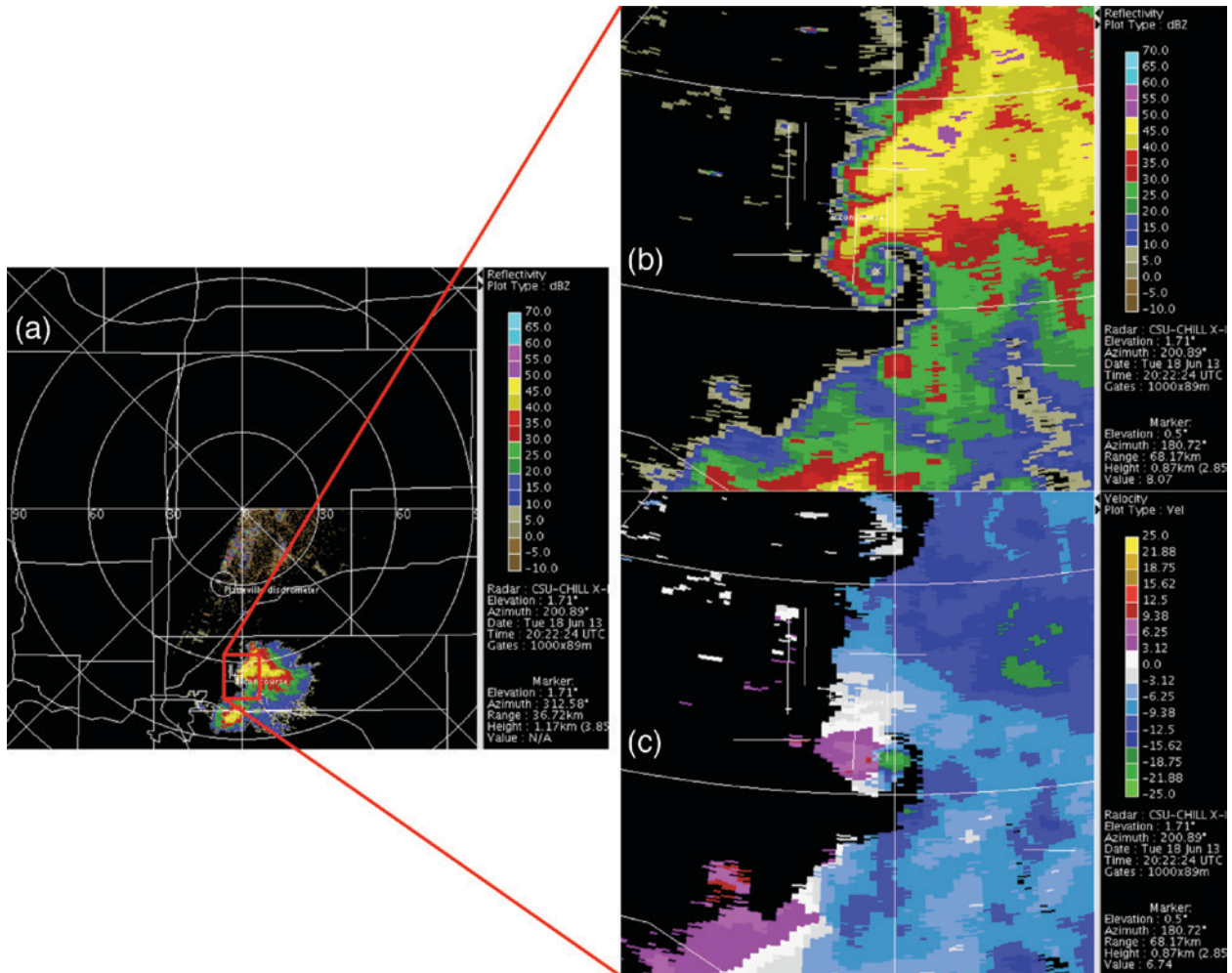


FIG. 18. General view and detailed view of a tornadic thunderstorm over Denver International Airport on 18 Jun 2013 as measured by the CSU-CHILL radar X-band component. (a) General Z view with the storm located around 70 km directly south of the radar. (b) Detailed Z view of the storm's associated hook echo. (c) Corresponding V field and collocated velocity couplet. Very small antenna beamwidth at X band (0.3°) allows for resolving with great detail a well-defined hook-echo signature of small diameter (less than 2 km) and associated velocity couplet at a far range (near 70 km). A small "x" marks the location of the center of the velocity couplet and hook-echo signatures.

S band, with high-quality polarimetric data at both frequencies. The high resolution at X band allows finescale features, not typically revealed by the S-band component data, to be resolved.

The CSU-CHILL radar is now operating as part of the Front Range Observational Network Testbed (FRONT) formed by the CSU-CHILL radar and the National Center for Atmospheric Research (NCAR) S- and Ka-band Polarimetric (SPolKa) radar. The latter facility is now operational approximately 40 km south of CSU-CHILL, forming a dual-Doppler, multifrequency polarimetric network. Requests for FRONT as a community observational facility are now being accepted as described online (www.eol.ucar.edu/observing_facilities/front). FRONT is also

located with coverage of the northeast Colorado Lightning Mapping Array (LMA), providing information on lightning flash rates and charge structures (<http://lightning.nmt.edu/colma/>). CSU-CHILL, FRONT, and the LMA network form a powerful means to study cloud dynamics, microphysics, and cloud electrification.

The CSU-CHILL radar is available for users via several request mechanisms. The request process can be found on the facility's web page (www.chill.colostate.edu/w/Facilities#Requesting_Use_of_the_Facility). Users may also access a large variety of archived datasets via the facility's Virtual CHILL (VCHILL) system, also available on the CSU-CHILL web page.

ACKNOWLEDGMENTS. This material is based upon work supported by the National Science Foundation under Cooperative Agreement AGS 1138116 and Colorado State University. L. Tolstoy, G. J. Huang, and M. Galvez assisted with data processing to create Figs. 11 and 12.

REFERENCES

- Andrić, J., M. Kumjian, D. Zrnić, J. Straka, and V. Melnikov, 2013: Polarimetric signatures above the melting layer in winter storms: An observational and modeling study. *J. Appl. Meteor. Climatol.*, **52**, 682–700, doi:10.1175/JAMC-D-12-028.1.
- Atlas, D., 1990: *Radar in Meteorology: Battan Memorial and 40th Anniversary Radar Meteorology Conference*. Amer. Meteor. Soc., 806 pp.
- , and F. H. Ludlam, 1961: Multi-wavelength radar reflectivity of hailstorms. *Quart. J. Roy. Meteor. Soc.*, **87**, 523–534, doi:10.1002/qj.49708737407.
- Bharadwaj, N., V. Chandrasekar, and F. Junyent, 2010: Signal processing system for the CASA Integrated Project I radars. *J. Atmos. Oceanic Technol.*, **27**, 1440–1460, doi:10.1175/2010JTECHA1415.1.
- Bringi, V. N., and V. Chandrasekar, 2001: *Polarimetric Doppler Weather Radar: Principles and Applications*. Cambridge University Press, 664 pp.
- , R. M. Rasmussen, and J. Vivekanandan, 1986a: Multiparameter radar measurements in Colorado convective storms. Part I: Graupel melting studies. *J. Atmos. Sci.*, **43**, 2545–2563, doi:10.1175/1520-0469(1986)043<2545:MRMICC>2.0.CO;2.
- , J. Vivekanandan, and J. D. Tuttle, 1986b: Multiparameter radar measurements in Colorado convective storms. Part II: Hail detection studies. *J. Atmos. Sci.*, **43**, 2564–2577, doi:10.1175/1520-0469(1986)043<2564:MRMICC>2.0.CO;2.
- , R. Hoferer, D. A. Brunkow, R. Schwerdtfeger, V. Chandrasekar, S. A. Rutledge, J. George, and P. C. Kennedy, 2011: Design and performance characteristics of the new 8.5-m dual-offset Gregorian antenna for the CSU–CHILL radar. *J. Atmos. Oceanic Technol.*, **28**, 907–920, doi:10.1175/2011JTECHA1493.1.
- Brunkow, D., V. N. Bringi, P. C. Kennedy, S. A. Rutledge, V. Chandrasekar, E. A. Mueller, and R. K. Bowie, 2000: A description of the CSU–CHILL National Radar Facility. *J. Atmos. Oceanic Technol.*, **17**, 1596–1608, doi:10.1175/1520-0426(2000)017<1596:ADOTCC>2.0.CO;2.
- Caylor, I. J., and V. Chandrasekar, 1996: Time-varying ice crystal orientation in thunderstorms observed with multiparameter radar. *IEEE Trans. Geosci. Remote Sens.*, **34**, 847–858, doi:10.1109/36.508402.
- Chandrasekar, V., M. Schwaller, M. Vega, J. Carswell, K. Mishra, R. Meneghini, and C. Nguyen, 2010: Scientific and engineering overview of the NASA dual-frequency dual-polarized Doppler radar (D3R) system for GPM ground validation. *2010 IEEE International Geoscience and Remote Sensing Symposium: Proceedings*, IEEE, 1308–1311.
- Eccles, P., 1979: Comparison of remote measurements by single- and dual-wavelength meteorological radars. *IEEE Trans. Geosci. Electron.*, **17**, 205–218, doi:10.1109/TGE.1979.294650.
- , and E. Mueller, 1971: X-band attenuation and liquid water content estimation by a dual-wavelength radar. *J. Appl. Meteor.*, **10**, 1252–1259, doi:10.1175/1520-0450(1971)010<1252:XBAALW>2.0.CO;2.
- , and D. Atlas, 1973: A dual-wavelength radar hail detector. *J. Appl. Meteor.*, **12**, 847–854, doi:10.1175/1520-0450(1973)012<0847:ADWRHD>2.0.CO;2.
- Gaussiat, N., H. Sauvageot, and A. Illingworth, 2003: Cloud water and ice content retrieval by multiwavelength radar. *J. Atmos. Oceanic Technol.*, **20**, 1264–1275, doi:10.1175/1520-0426(2003)020<1264:CLWAIC>2.0.CO;2.
- Herzegg, P., and A. Jameson, 1992: Observing precipitation through dual-polarization radar measurements. *Bull. Amer. Meteor. Soc.*, **73**, 1365–1374, doi:10.1175/1520-0477(1992)073<1365:OPTDPR>2.0.CO;2.
- Jameson, A., and R. Srivastava, 1978: Dual-wavelength Doppler radar observations of hail at vertical incidence. *J. Appl. Meteor.*, **17**, 1694–1703, doi:10.1175/1520-0450(1978)017<1694:DWDROO>2.0.CO;2.
- , and A. Heymsfield, 1980: Hail growth mechanisms in a Colorado hailstorm. Part I: Dual-wavelength radar observations. *J. Atmos. Sci.*, **37**, 1763–1778, doi:10.1175/1520-0469(1980)037<1763:HGMIAIC>2.0.CO;2.
- Kennedy, P., and S. Rutledge, 2011: S-band dual-polarization radar observations of winter storms. *J. Appl. Meteor. Climatol.*, **50**, 844–858, doi:10.1175/2010JAMC2558.1.
- Knight, C., and L. Miller, 1993: First echoes from cumulus clouds. *Bull. Amer. Meteor. Soc.*, **74**, 179–188, doi:10.1175/1520-0477(1993)074<0179:FR EFCC>2.0.CO;2.
- Kumjian, M. R., S. A. Rutledge, R. M. Rasmussen, P. C. Kennedy, and M. Dixon, 2014: High-resolution polarimetric radar observations of snow-generating cells. *J. Appl. Meteor. Climatol.*, **53**, 1636–1658, doi:10.1175/JAMC-D-13-0312.1.

- Levenberg, K., 1944: A method for the solution of certain problems in least squares. *Quart. Appl. Math.*, **2**, 164–168.
- Marquardt, D., 1963: An algorithm for least-squares estimation of nonlinear parameters. *SIAM J. Appl. Math.*, **11**, 431–441, doi:10.1137/0111030.
- Park, S., M. Maki, K. Iwanami, V. Bringi, and V. Chandrasekar, 2005: Correction of radar reflectivity and differential reflectivity for rain attenuation at X band. Part II: Evaluation and application. *J. Atmos. Oceanic Technol.*, **22**, 1633–1655, doi:10.1175/JTECH1804.1.
- Rinehart, R., and J. Tuttle, 1982: Antenna beam patterns and dual-wavelength processing. *J. Appl. Meteor.*, **21**, 1865–1880, doi:10.1175/1520-0450(1982)021<1865:ABPADW>2.0.CO;2.
- Snyder, J., H. Bluestein, V. Venkatesh, and S. Frasier, 2013: Observations of polarimetric signatures in supercells by an X-band mobile Doppler radar. *Mon. Wea. Rev.*, **141**, 3–29, doi:10.1175/MWR-D-12-00068.1.
- Trömel, S., M. R. Kumjian, A. Ryzhkov, C. Simmer, and M. Diederich, 2013: Backscatter differential phase—Estimation and variability. *J. Appl. Meteor. Climatol.*, **52**, 2529–2548, doi:10.1175/JAMC-D-13-0124.1.
- Tuttle, J., V. Bringi, H. Orville, and F. Kopp, 1989: Multiparameter radar study of a microburst: Comparison with model results. *J. Atmos. Sci.*, **46**, 601–620, doi:10.1175/1520-0469(1989)046<0601:MRSOAM>2.0.CO;2.
- Ulbrich, C., and D. Atlas, 1982: Hail parameter relations: A comprehensive digest. *J. Appl. Meteor.*, **21**, 22–43, doi:10.1175/1520-0450(1982)021<0022:HPRACD>2.0.CO;2.
- Vivekanandan, J., G. Zhang, and M. Politovich, 2001: An assessment of droplet size and liquid water content derived from dual-wavelength radar measurements to the application of aircraft icing detection. *J. Atmos. Oceanic Technol.*, **18**, 1787–1798, doi:10.1175/1520-0426(2001)018<1787:AAODSA>2.0.CO;2.
- Wang, Y., and V. Chandrasekar, 2009: Algorithm for estimation of the specific differential phase. *J. Atmos. Oceanic Technol.*, **26**, 2565–2578, doi:10.1175/2009JTECHA1358.1.

NEW! PRINT & CD FORMATS

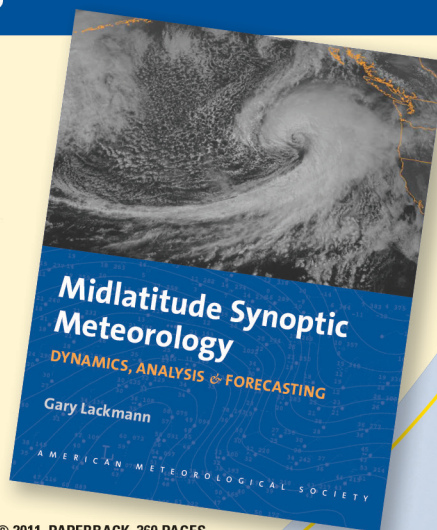
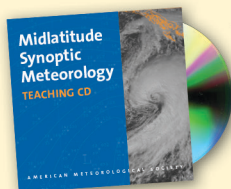
“Professor Lackmann has prepared an excellent synthesis of quintessential modern midlatitude synoptic-dynamic meteorology.”

—LANCE BOSART, Distinguished Professor, Department of Atmospheric and Environmental Sciences, The University of Albany, State University of New York

Midlatitude Synoptic Meteorology: Dynamics, Analysis, and Forecasting

GARY LACKMANN

The past decade has been characterized by remarkable advances in meteorological observation, computing techniques, and data-visualization technology. *Midlatitude Synoptic Meteorology* links theoretical concepts to modern technology and facilitates the meaningful application of concepts, theories, and techniques using real data. As such, it both serves those planning careers in meteorological research and weather prediction and provides a template for the application of modern technology in the classroom.



© 2011, PAPERBACK, 360 PAGES
Digital edition also available
ISBN: 978-1-878220-10-3
AMS CODE: MSM
LIST \$100 MEMBER \$75
STUDENT \$65

Instructors: *Midlatitude Synoptic Teaching CD*, containing over 1,000 lecture slides, is now available!

AMS BOOKS

RESEARCH APPLICATIONS HISTORY

www.ametsoc.org/amsbookstore 617-226-3998